2023 IEEE/ASME International Conference on Advanced Intelligent Mechatronics (AIM)
June 28-30, 2023. Seattle, Washington, USA

Analytical Design Methodology based on Distributed Current Source Models for Parametric Study of a Three-DOF Planar Motor

Zixin Que, and Kok-Meng Lee*, *Life Fellow*, *IEEE*

***Abstract*— This paper presents a design method based on distributed current source (DCS) that discretizes the permanent magnets (PMs) and electromagnets (EMs) into elemental current sources and derives the magnetic field and current-force models for design analyses of a 3-degree-of-freedom (3-DOF) planar motor with redundant inputs. The DCS models have been verified by comparing them with exact solutions and commercial finite element analysis (FEA). The results show that the DCS models are accurate (within 2.5% of exact solutions) and computationally efficient (a three-order improvement over FEA). As an illustration, the analytically derived DCS models are employed to analyze the geometrical constraints and parametric effects on the PM/EM layout and forces/torque performance of a 3-DOF planar motor. Using singular value decomposition, two designs are numerically evaluated. With the closed-form DCS models, the loci of the best/worst manipulability ellipsoids are graphically presented.**

I. Introduction

Multi-DOF PM motors play an important role in a wide variety of applications ranging from traditional to emerging human-centered industries; the latter demands new ways to design devices that can accommodate bio-joint variations [1][2]. Although accurate electric motors are widely available at a reasonably low cost, they are often designed to operate at a fixed rotational axis, and generally not for rehabilitation like exoskeletons that help early stroke patients lacking force perception perform in-bed exercises [3][4]. In response to this need, this paper presents a field-based method for analyzing the parametric effects on the forces/torque of a 3-DOF planar motor characterized by redundant inputs to accommodate translational motions while flexing in the sagittal plane.

Muti-DOF PM motor designs involve modeling the current-force relationship in the presence of a magnetic field; both the forward/inverse models are needed. The forward model uniquely determines the forces/torque at a given position/orientation for a set of specified inputs, but its inverse solutions for a planar motor with redundant inputs (>3) will have multiple solutions. Although the Biot-Savart law and Lorentz force equation for solving the magnetic field/force analytically are well established, they are limited to geometrically simple problems with ideal boundary conditions. In [5][6], a numerical curve fitting or the first harmonic of the magnetic flux density (MFD) was used to analyze the MFD field of a 2-DOF PM array planar motor; this approach ignores higher harmonics as well as boundary effects resulting in force ripples due to modeling errors and must be suppressed, for example, utilizing feedback control [7] or an optimization algorithm [8]. For magnetic systems with complex geometry, FEA has been most frequently employed because commercial software and related techniques are available. FEA can be combined with topology optimization to find the best layout of different materials (PM, EM, and iron), boundary/shape, and magnetization direction [9]. The tradeoff is that FEA must incorporate air space in its solution domain, resulting in low efficiency and numerical errors. Alternatively, the magnetic problems can be formulated using the distributed current source (DCS) method originally developed [10] as a general and physically intuitive method for modeling the magnetic fields of an electromagnetic system, which has been extended to solve problems involving eddy-current induced in a conductor [11]. The DCS method has also been developed to design drive systems for high-speed capsule trains [12] where the coil shape of high-temperature superconducting magnets is topologically optimized concerning cost/performance. Other approaches have also been proposed to analyze material effects on magnetic forces [13][14].

Motivated by the attractive features of the DCS method that formulates the magnetic field and solves its solutions in closed form, this paper extends the method to streamline the design process of a 3-DOF planar motor with redundant inputs. The remainder of this paper offers the following: *Section II* begins with the DCS model to describe the current-force relationship of a 3-DOF planar motor. As an illustration, both the force model and its inverse solutions are derived for a motor design consisting of cylindrical PMs and annular EMs to provide the basis for studying its parametric effects using eigenvalue decomposition and manipulability ellipsoids [15]. In *Section III*, the DCS models are verified with exact solutions and applied to study the parametric effects on the force and torque performance of a planar motor. The findings are summarized in *Section IV*.

II. DCS-Based Force-Current Models

Figure 1(a) shows the CAD model of a 3-DOF planar motor, where the rotor houses two rings of N_e EMs sandwiched between two sets of $2N_p$ PMs. In Fig. 1(a) where (*XYZ*, *xyz*) are the coordinate frames at the centers of the (stator, rotor), both the (PMs, EMs) are evenly distributed on a circle with radii (r_s, r_r) and angular spacing of (ϕ_p, ϕ_e). The (upper, lower) rings, which are discriminated by the subscripts (+, −) for simplicity in mathematical derivations, are geometrically symmetric about the *XY* and *xy* planes with displacement (H, h) as shown in Fig. 1(b) where $\mathbf{J}_m$ is the current (volume) density of the m^{th} EM and $\mathbf{M}_n$ is the magnetization vector of the n^{th} PM.

In the stator *XYZ* coordinates, the (m^{th} EM, n^{th} PM) centers are defined by their position vectors (1a, b) where m =1, 2, …, N_e and n =1, 2, …, $2N_p$:

$$\mathbf{P}_{n\pm}\big|_{\text{PM}} = \begin{bmatrix} r_s\cos\phi_{pn} & r_s\sin\phi_{pn} & \pm H \end{bmatrix}^{\text{T}} \tag{1a}$$

This work was supported in part by the National Science Foundation of China under Grant U1713204, and in part by the U. S. National Science Foundation CMMI-166270. **Corresponding author*: *Kok-Meng Lee.*

Zixin Que is with the State Key Lab. of Dig. Manuf. Equip. and Tech., Huazhong Univ. of Sci. and Tech., Wuhan Hubei 430074, China. (e-mail: d202080220@hust.edu.cn).

Kok-Meng Lee is with the George W. Woodruff School of Mechanical Engineering, Georgia Institute of Technology, Atlanta, GA 30332, USA (e-mail: kokmeng.lee@me.gatech.edu).

$$\mathbf{P}_{m\pm}(X_r, Y_r, \theta)\big|_{\text{EM}} = [\mathbf{R}_Z(\theta)]\begin{bmatrix} r_r \cos\phi_{em} \\ r_r \sin\phi_{em} \\ \pm h \end{bmatrix} + \mathbf{P}_c \tag{1b}$$

where $\phi_{pn} = (n-1)\phi_p$, $\phi_{em} = (m-1)\phi_e$,

$$[\mathbf{R}_Z(\theta)] = \begin{bmatrix} \cos\theta & -\sin\theta & 0 \\ \sin\theta & \cos\theta & 0 \\ 0 & 0 & 1 \end{bmatrix} \text{ and } \mathbf{P}_c = \begin{bmatrix} X_c \\ Y_c \\ Z_c = 0 \end{bmatrix}. \tag{1c~f}$$

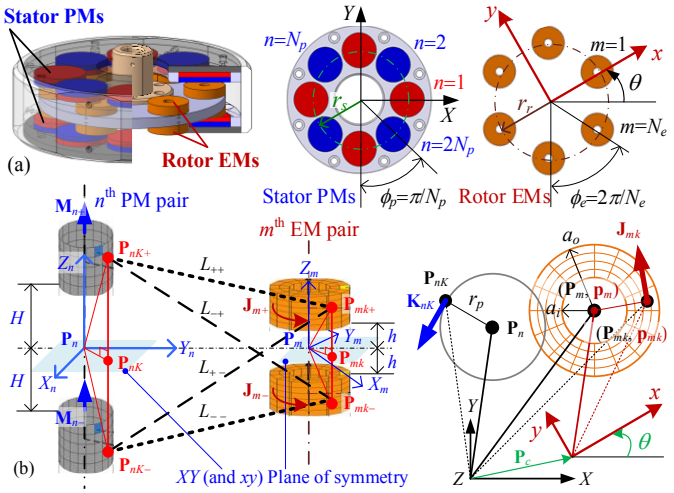

Fig. 1. Schematics illustrating three-DOF planar motor. (a) CAD model and geometrical layouts of rotor EMs and stator PMs. (b) The MFDs contributed by the SCD sources of a PM-pair at the VCD sources of an EM-pair.

For analyzing the electromagnetic field/forces/torque using the distributed current source (DCS) method[10], the PM and EM are modeled as surface-current-density (SCD) **K** and volume-current-density (VCD) **J** sources, respectively. The DCS method decomposes the n^{th} PM's circumferential surface S_p into N_K elemental SCD $\mathbf{K}_{nK}$ (area s_K where K=1, 2, …, N_K), and the EM's volume V_e into N_k elemental VCD $\mathbf{J}_{mk}$ where k=1, 2, …, N_k. The PM's MFD field can then be computed using superposition, reducing the Biot-Savart integral for computing the stator's MFD $\mathbf{B}_s$ at the point-of-interest $\mathbf{P}$ to a summation of cross-products $\mathbf{K}_{nK}\times(\mathbf{P}-\mathbf{P}_{nK})$. Similarly, the volume integral for calculating the Lorentz force on the rotor is reduced to a sum of the elemental cross-products ($\mathbf{J}_{mk}\times\mathbf{B}_s$) over the N_k elements.

To facilitate design, the geometrical parameters are normalized to the PM radius r_p in (2):

$$\frac{(r_s, r_r)}{(\rho_s, \rho_r) r_p} = \frac{(H, h)}{(\rho_H, \rho_h) r_p} = \frac{(l_p, l_e)}{(\rho_p, \rho_e) r_p} = \frac{(a_o, a_i)}{(\rho_o, \rho_i) r_p} = (1,\ 1) \tag{2}$$

For consistency, the position, MFD, SCD, VCD, and force vectors are normalized accordingly in (3a~e) in terms of the characteristic parameters defined in (3f~g) where μ_0 is the permeability of free space and J_o is a nominal current density flowing through the EMs' cross-sectional area:

$$\frac{\mathbf{P}}{r_p \bar{\mathbf{P}}} = \frac{\mathbf{B}}{B_o \bar{\mathbf{B}}} = \frac{\mathbf{K}}{M_o \bar{\mathbf{K}}} = \frac{\mathbf{J}}{J_o \bar{\mathbf{J}}} = \frac{\mathbf{f}}{f_o \bar{\mathbf{f}}} = \mathbf{I}_{3\times 3} \tag{3a~e}$$

where $B_o = \mu_0 M_o$ and $f_o = B_o J_o V_e$. (3f~g)

A. DCS-based Magnetic Force-Current Model

Figure 1(b) defines the coordinate systems, parameters, and variables for modeling the magnetic force acting on the m^{th} current-carrying EM-pair ($\mathbf{J}_m$ at $\mathbf{P}_m$) in the MFD field of the n^{th} PM-pair (SCD $\mathbf{K}_n$ at $\mathbf{P}_n$); both are uniform across the thickness. Given the normalized MFD field of the stator PMs in (4a), the magnetic force/torque on the rotor can then be computed from (4b, c) by summing the individual forces $\mathbf{f}_{mk\pm}$ between the SCD elements $\mathbf{P}_{nK\pm}$ of the stator PMs and the VCD elements $\mathbf{P}_{mk\pm}$ of the rotor EMs:

$$\bar{\mathbf{B}}_s(\bar{\mathbf{P}}_{mk\pm}) = \frac{\rho_p}{2}\sum_{n=1}^{2N_p}\sum_{K=1}^{N_K}\left[\bar{s}_{nK}\bar{\mathbf{K}}_{nK}\times\left(\frac{\bar{\mathbf{L}}_{\pm+}}{\bar{L}_{\pm+}^3} + \frac{\bar{\mathbf{L}}_{\pm-}}{\bar{L}_{\pm-}^3}\right)\right] \tag{4a}$$

$$\bar{\mathbf{f}} = \sum_{m=1}^{N_e}\sum_{k=1}^{N_k}\left(\bar{v}_{mk}\bar{\mathbf{J}}_{mk}\times\left[\bar{\mathbf{B}}_s(\bar{\mathbf{P}}_{mk+}) + \bar{\mathbf{B}}_s(\bar{\mathbf{P}}_{mk-})\right]\right) \tag{4b}$$

$$\bar{\boldsymbol{\tau}} = \frac{\boldsymbol{\tau}}{r_p f_0} = \sum_{m=1}^{N_e}\sum_{k=1}^{N_k}\left[\begin{matrix}(\bar{\mathbf{P}}_{mk+} - \bar{\mathbf{P}}_c)\times\bar{\mathbf{f}}_{mk+} + \\ (\bar{\mathbf{P}}_{mk-} - \bar{\mathbf{P}}_c)\times\bar{\mathbf{f}}_{mk-}\end{matrix}\right] \tag{4c}$$

where $\bar{\mathbf{L}}_{\pm+} = \bar{\mathbf{P}}_{mk\pm} - \bar{\mathbf{P}}_{nK+}$, $\bar{\mathbf{L}}_{\pm-} = \bar{\mathbf{P}}_{mk\pm} - \bar{\mathbf{P}}_{nK-}$ (4d, e)

and $\bar{\mathbf{P}}_{mk\pm} = [\mathbf{R}_Z(\theta)](\bar{\mathbf{p}}_m + \bar{\mathbf{p}}_{mk\pm}) + \bar{\mathbf{P}}_c$ (4f)

In (4a, b), the (area s_{nK}, volume v_{mk}) of the (n^{th} PM, m^{th} EM) are normalized ($\bar{s}_{nK} = s_{nK}/S_p$, $\bar{v}_{mk} = v_{mk}/V_e$).

As illustrated in Fig. 1(b), the PM elements at $\mathbf{P}_{nK\pm}$ and EM elements at $\mathbf{P}_{mk\pm}$ (4d, e) form a trapezoid symmetric about the XY plane implying (5a~c) where L is the length of $\mathbf{L}$:

$$L_{++} = L_{--} \text{ and } L_{+-} = L_{-+} \tag{5a, b}$$

$$(\bar{\mathbf{P}}_{mk+} + \bar{\mathbf{P}}_{mk-}) - (\bar{\mathbf{P}}_{nK+} + \bar{\mathbf{P}}_{nK-}) = 2(\bar{\mathbf{P}}_{mk} - \bar{\mathbf{P}}_{nK}) \tag{5c}$$

Substituting (4a) into (4b) along with the properties (5a~c), the normalized magnetic force can be rewritten as

$$\bar{\mathbf{f}}(X_c, Y_c, \theta) = \rho_p\sum_{m,n}\sum_{k,K}\left(\bar{v}_{mk}\bar{\mathbf{J}}_{mk}\times\left[\bar{s}_{nK}\bar{\mathbf{K}}_{nK}\times\frac{(\bar{\mathbf{P}}_{mk} - \bar{\mathbf{P}}_{nK})}{\bar{L}_{eq}^3}\right]\right)$$

where $\bar{L}_{eq}^{-3} = \bar{L}_{++}^{-3} + \bar{L}_{+-}^{-3}$ (6a, b)

Although the PMs' MFD at the EMs (4a) are three dimensional (3D), the relative displacement ($\mathbf{P}_{mk}$–$\mathbf{P}_{nK}$) and the elemental (SCD $\mathbf{K}_{nK}$, VCD $\mathbf{J}_{mk}$) are planar (Fig. 1b). Hence, the force in (6a) has no Z-component at Z_c=0 but creates a moment of the Z-axis, which can be computed from the sum of the elemental cross-product ($\mathbf{P}_{mk}$–$\mathbf{P}_c$)×$\mathbf{f}_{mk}$.

For a given design (known $\mathbf{P}_{n\pm}$ and $\mathbf{p}_{m\pm}$), $\mathbf{P}_{m\pm}$ can be determined from the forward kinematics (1a, b); hence the normalized forces/torque of the 3-DOF planar motor can be written compactly in matrix form:

$$\mathbf{F}(\mathbf{q}) = [\mathbf{A}(\mathbf{q})]_{3\times N_e}\,\mathbf{u}_{N_e\times 1};\ [\mathbf{A}]_{3\times N_e} = [\boldsymbol{\alpha}_1 \cdots \boldsymbol{\alpha}_m \cdots \boldsymbol{\alpha}_{N_e}]$$

where $\mathbf{q}^{\mathrm{T}} = [\bar{X}_c\ \bar{Y}_c\ \theta]$, $\mathbf{F}^{\mathrm{T}} = [\bar{f}_X\ \bar{f}_Y\ \bar{\tau}_Z]$, and $\mathbf{u}^{\mathrm{T}} = [u_1 \cdots u_m \cdots u_{N_e}]$ (7a~e)

In (7b), the m^{th} column vector $\boldsymbol{\alpha}_m$ ($\in\mathbb{R}^{3\times 1}$) of the force-current matrix [**A**] is position/orientation **q** dependent and a function of the PM/EM layout/geometry.

B. Force-Current Coefficient Vector $\boldsymbol{\alpha}_m$

Without loss of generality, the column-vector $\boldsymbol{\alpha}_m$ of [**A**] in (7a) is illustrated with cylindrical PMs and annular EMs characterized by the following properties:

– PM (l_p thick, radius r_p, and $\mathbf{M}$=M_o[0 0 ±1]$^{\mathrm{T}}$: The SCD is uniformly discretized circumferentially and axially into N_K equal-area ($S_p = 2\pi r_p l_p$, $\bar{s}_{nK} = 1/N_K$) elemental SCD sources:

$$\bar{\mathbf{K}}_{nK} = \mathbf{K}_{nK}/M_o = (-1)^{n-1}\left[-\sin\varphi_{nK}\ \ \cos\varphi_{nK}\ \ 0\right]^{\mathrm{T}} \tag{8}$$

– EM with (outer a_o, inner a_i) radii, l_e thick, and $|\mathbf{J}_m|$=$u_m J_o$:

$$\bar{\mathbf{J}}_{mk} = \mathbf{J}_{mk}/J_o = u_m\left[-\sin(\varphi_{mk} + \theta)\ \ \cos(\varphi_{mk} + \theta)\ \ 0\right]^{\mathrm{T}}$$

where $J_o = \dfrac{I_o N_T}{l_e (a_o - a_i)}$ and $I_o = 1$ Ampere. (9a, b)

The VCD is discretized uniformly in the circumferential and axial directions but decreasingly radially into equal-volume N_k elemental VCD sources ($V_e = \pi(a_o^2 - a_i^2) l_e$, $\bar{v}_{mk} = 1/N_k$). In (9a), $(a_o - a_i)$ is discretized radially into n_{Rad} layers, and its radial position (normalized to r_p) of the j^{th} elemental VCD source between two adjacent edges is described by

$$\rho_j = \left(\sqrt{\rho_i^2 + (j-1)\frac{\rho_o^2 - \rho_i^2}{n_{Rad}}} + \sqrt{\rho_i^2 + j\frac{\rho_o^2 - \rho_i^2}{n_{Rad}}} \right) \Big/ 2 \quad (9c)$$

Using (4f) and (6a, b), the column vectors of the force-current matrix [**A**] are derived for a design with known [ρ_p, (ρ_s, ϕ_{pn})] and [ρ_e, (ρ_r, ϕ_{em})] at a specified $(\bar{X}_c, \bar{Y}_c, \theta)$:

$$\boldsymbol{\alpha}_m \left(\bar{X}_c, \bar{Y}_c, [\mathbf{R}_{2\times2}(\theta)] \right) = \frac{\rho_p}{N_k N_K} \sum_{k=1}^{N_k} \left(\begin{bmatrix} [\mathbf{R}_{2\times2}(\theta)] \begin{bmatrix} \cos\varphi_{mk} \\ \sin\varphi_{mk} \end{bmatrix} \\ \rho_r \sin(\varphi_{mk} - \phi_{em}) \end{bmatrix} \sum_{n=1}^{2N_p} \sum_{K=1}^{N_K} \frac{(-1)^{n-1} \mathcal{K}}{\bar{L}_{eq}^3} \right) \quad (10a)$$

where $[\mathbf{R}_{2\times2}(\theta)] = \begin{bmatrix} \cos\theta & -\sin\theta \\ \sin\theta & \cos\theta \end{bmatrix}$, (10b)

$$\mathcal{K}\left(\bar{X}_c, \bar{Y}_c, [\mathbf{R}_{2\times2}(\theta)] \right) = 1 + [\cos\varphi_{nK} \quad \sin\varphi_{nK}] \left(\begin{bmatrix} C_{pn} \\ S_{pn} \end{bmatrix} - [\mathbf{R}_{2\times2}(\theta)] \begin{bmatrix} C_{mk} \\ S_{mk} \end{bmatrix} \right), \quad (10c)$$

$$\begin{bmatrix} C_{pn}(\bar{X}_c, \bar{Y}_c) \\ S_{pn}(\bar{X}_c, \bar{Y}_c) \end{bmatrix} = \rho_s \begin{bmatrix} \cos\phi_{pn} \\ \sin\phi_{pn} \end{bmatrix} - \begin{bmatrix} \bar{X}_c \\ \bar{Y}_c \end{bmatrix}, \text{ and} \quad (10d)$$

$$\begin{bmatrix} C_{mk} \\ S_{mk} \end{bmatrix} = \rho_r \begin{bmatrix} \cos\phi_{em} \\ \sin\phi_{em} \end{bmatrix} + \rho_{mk} \begin{bmatrix} \cos\varphi_{mk} \\ \sin\varphi_{mk} \end{bmatrix} \quad (10e)$$

In (10e), the normalized radial position ρ_{mk} has been defined in (9c) where the subscript j=mk. From the distance vectors in (11a) and their lengths in (11b, c), $\bar{L}_{eq}^{-3}$ defined in (6b) can be derived in (11c):

$$\bar{\mathbf{L}}_{+\pm} = \begin{bmatrix} \bar{L}_X \\ \bar{L}_Y \\ \bar{L}_{Z+\pm} \end{bmatrix} = \begin{bmatrix} [\mathbf{R}_{2\times2}(\theta)] \begin{bmatrix} C_{mk} \\ S_{mk} \end{bmatrix} - \begin{bmatrix} C_{pn} + \cos\varphi_{nK} \\ S_{pn} + \sin\varphi_{nK} \end{bmatrix} \\ \bar{z}_{mk} \mp \bar{z}_{nK} \end{bmatrix}$$

where $\bar{L}_{+\pm} = \sqrt{\bar{L}_\Sigma^2 \mp 2\bar{z}_{mk}\bar{z}_{nK}}$ and $\bar{L}_\Sigma^2 = \bar{L}_X^2 + \bar{L}_Y^2 + \bar{z}_{mk}^2 + \bar{z}_{nK}^2$

$$\text{hence, } \bar{L}_{eq}^{-3} = \frac{\left(\bar{L}_\Sigma^2 - 2\bar{z}_{mk}\bar{z}_{nK}\right)^{3/2} + \left(\bar{L}_\Sigma^2 + 2\bar{z}_{mk}\bar{z}_{nK}\right)^{3/2}}{\left(\bar{L}_\Sigma^4 - 4\bar{z}_{mk}^2\bar{z}_{nK}^2\right)^{3/2}} \quad (11a\sim d)$$

Given the force-current coefficient vectors $\boldsymbol{\alpha}_m$ (where m=1, …, N_k), the force vector **F** can be uniquely determined by computing the *forward force model* (7a~e) for a specified displacement vector **q**.

C. Inverse Model and Design Optimization

Theoretically, three or more independent inputs ($N_e \geq 3$) are needed to provide three-DOF planar motion. However, if the actuation system has redundant inputs ($N_e > 3$), the inverse solutions to the forward model (7a~e) are nonunique but can be solved for a least-norm solution that minimizes $\|\mathbf{u}^T\mathbf{u}\|$ subject to the constraint (7a). The optimal solution can be derived via the Lagrange multiplier leading to the right pseudoinverse (12):

$$\mathbf{u} = \mathbf{A}^T \left(\mathbf{A}\mathbf{A}^T \right)^{-1} \mathbf{F} \quad (12)$$

For a specified rotor position/orientation, the 3-DOF planar motor is in a singular state (losing one or more DOF) if rank(**A**)<3. To optimize the manipulability of the planar motor by design, this problem is analyzed using singular value decomposition (SVD). The SVD is formulated in terms of $\mathbf{A}\mathbf{A}^T$ characterized by eigenvalues ($\lambda_1 \geq \lambda_2 \geq \lambda_3$) in $\boldsymbol{\Lambda}$ and singular values $\sigma_i = \sqrt{\lambda_i}$ where i=1,2,3:

$$\mathbf{A} = \mathbf{U}\boldsymbol{\Sigma}\mathbf{V}^T \text{ and } \mathbf{A}\mathbf{A}^T = \mathbf{U}\boldsymbol{\Lambda}\mathbf{U}^T \quad (13a, b)$$

$$\text{where } \boldsymbol{\Sigma} = \left[\text{diag}(\sigma_1 \;\; \sigma_2 \;\; \sigma_3) \;\; \mathbf{0} \right] \quad (13c)$$

In (13a, b), the columns of [**U**, **V**] are the orthogonal eigenvectors of ($\mathbf{A}\mathbf{A}^T$, $\mathbf{A}^T\mathbf{A}$). The design evaluation of the planar motor can then be visualized graphically in terms of a manipulability ellipsoid characterized by the eigenvector **U**. For quantitative evaluation, two measures are defined in (14a, b) where the ellipsoid-flattening E_F measures its directional uniformity, and scalar E_V is a measure of its volume:

$$E_F = 1 - \text{cond}^{-1}(\mathbf{A}) \text{ where } \text{cond}(\mathbf{A}) = \sigma_1 / \sigma_3 \quad (14a)$$

$$E_V = \sqrt{\det(\mathbf{A}\mathbf{A}^T)} = \sigma_1\sigma_2\sigma_3 = (3/4\pi) V_{\text{ellipsoid}} \quad (14b)$$

From (7b), $\mathbf{A}\mathbf{A}^T = \sum_{m=1}^{N_e} \boldsymbol{\alpha}_m \boldsymbol{\alpha}_m^T$ (14c)

III. Results and Discussion

The forward/inverse models describing the force-current relationship of a 3-DOF planar motor and manipulability ellipsoid for parametric analyses are best illustrated numerically. Two numerical studies are performed:

- Presented in *Section III.A*, the 1st study has a *three-folded* objective: It begins with verifying the DCS (MFD, force) models with the exact solutions derived from the Biot- Savart law and Lorentz force integral to provide the ground truths for comparison. Next, the discretization effects on computation errors and time are analyzed. Thirdly, the effectiveness of the DCS models is evaluated by comparing them with FEA results simulated using commercial FEA software (COMSOL) in terms of the root-mean-square error (RMSE) and computation time.
- With a CAD model illustrating the design concept of a prototype three-DOF planar motor, *Section III.B* identifies the key parameters significantly influencing its PM/EM layouts and numerically analyzes the effects of the identified parameters on the force/torque characteristics studies using the design theory described in *Section II*.

A. DCS Model Verification with FEA Model

The accuracy and efficiency of the DCS models are evaluated by comparing their predictions with COMSOL simulations and analytically derived solutions. The results comparing the MFD of an axially magnetized cylindrical PM (for which the exact solution along the magnetizing axis is available in closed form) and the Lorentz force for the fundamental configuration (Fig. 1b) are presented in *Sections A.1* and *A.2* and discussed in *Section A.3*.

A.1 DCS MFD field model

As described in *Section II.B*, the DCS method discretizes the PM into N_K equal-area elemental SCD sources. The parametric values of the DCS and FEA models used in the evaluation are listed in Table I, where three DCS (PM1, 2, 5) models are used to study the effects of discretization (N_K=1×10, 2×20, 5×50) on the computation effectiveness. Unlike the DCS model, the 3D FEA meshes must include a sufficiently large air domain around the magnetic system (Table I), where the

tetrahedrons are automatically created by COMSOL. To ensure sufficient accuracy without sacrificing computation time, the element lengths of the tetrahedrons for the PM are smaller than 1mm, and those for the air domain are predefined in the range of 0.4 to 5mm. The results are summarized in Fig. 2 and Table I.

TABLE I. PARAMETERS USED IN NUMERICAL VERIFICATION

PM: $\mu_0 M_o$=1.44 T, r_p=10 mm, $\gamma=2r_p/l_p$=4

DCS	SCD, N_K = $n_{Axi} \times n_{Circ}$	Surf area s_K (mm^2)	RMSE (mT)	Comp. Time (s)
PM1	1 × 10	31.4	2.4	0.039
PM2	2 × 20	7.85	0.58	0.045
PM5	5 × 50	1.26	0.093	0.086
FEA	**Tetrahedron (free) 151835**		7.9	23
	Air Domain 100×100×100 mm (Predefined: 0.4~5 mm) 125,806 elements (83%)		**PM Domain** (Custom: Max 1 mm) 26,029 elements (17%)	

CPU: AMD Ryzen 7 with Radeon Graphics 3.20GHz, 16GB RAM.
MATLAB R2022a with Parallel Computing Toolbox.
COMSOL Multiphysics 6.0 with AC/DC magnetic fields.
*Average computation time for 10 simulations.

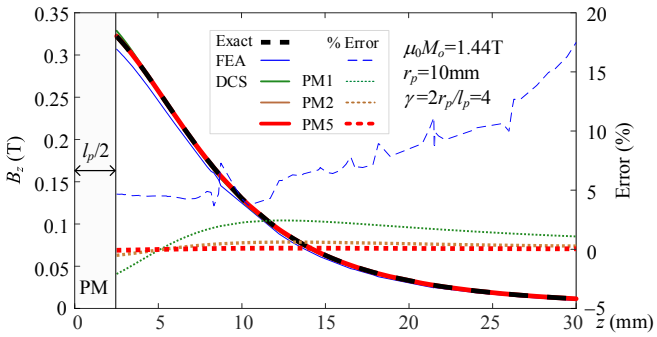

Fig. 2. DCS and FEA computed MFD fields of the PM and their errors relative to solutions derived from the Biot-Savart integral.

Figure 2 compares the MFD fields of the PM, where the exact solution (15) for verification in terms of the % Error (16) is derived from the Biot-Savart integral [16]:

$$\frac{B_Z(\bar{Z})}{\mu_0 M_o} = \frac{1}{2}\left[\frac{|B_+|}{A_+} - \frac{|B_-|}{A_-} + c\right] \text{ where } c = \begin{cases} 0 & \text{if } |\bar{Z}| \geq 1 \\ 2 & \text{if } |\bar{Z}| < 1 \end{cases} \quad (15)$$

$$\bar{Z} = 2z/l_p,\ \gamma = 2r_p/l_p;\ A_\pm = \sqrt{\gamma^2 + B_\pm^2} \text{ and } |B_\pm| = |\bar{Z} \pm 1|.$$

$$\%\ \text{Error} = 100 \times [\text{Exact} - \text{DCS (or FEA)}] / \text{Exact} \quad (16)$$

The DCS models are numerically evaluated in Table I in terms of the root mean square error (RMSE) defined in (17) over N data and computational time (seconds):

$$\text{RMSE} = \sqrt{\|\text{Exact} - \text{DCS (or FEA)}\|_2^2 / N} \quad (17)$$

A.2 DCS MFD field model

The effectiveness of the DCS model (*Section II.B*) for computing the force $\mathbf{F}_{PM}$ acting on the EM-pair (through which the current density $\mathbf{J}_{PM}$ flows) in the MFD field $\mathbf{B}_{PM}$ of the axially magnetized PM-pair is evaluated by comparing its force predictions with the force simulated using the COMSOL FEA model (Fig. 3). As for the DCS-modeled PM (Table I), the EM is similarly discretized but into N_k elemental VCD sources of equal volumes defined in (9a) to (9e). The parametric values of the DCS-modeled EMs and the 3D FEA model for simulating the fundamental configuration (Fig. 1b) are listed in Table II. As a ground truth for verification, the Lorentz force is calculated using the volume integral (18a) where (**R**', **R**) are the (source, observed) points for computing $\mathbf{B}_{PM}$ in the Biot-Savart's surface integral (18b):

$$\mathbf{F}_{EM} = \iiint_{V_{EM}} (\mathbf{J}_{EM} \times \mathbf{B}_{PM})\, dV \quad (18a)$$

$$\text{where } \mathbf{B}_{PM} = \frac{\mu_0 M_o}{4\pi} \iint_{S_{top} - S_{bot}} \frac{\mathbf{R} - \mathbf{R}'}{|\mathbf{R} - \mathbf{R}'|^3} dS \quad (18b)$$

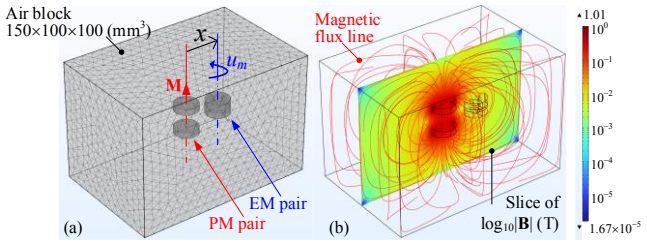

Fig. 3. FEA force simulation. (a) Solution domains and COMSOL meshes. (b) COMSOL simulated magnetic field.

The DCS-predicted forces are verified by the integral solutions (18a, b) and compared with COMSOL simulation in Fig. 4. The discretization effects of the DCS models on its effectiveness (evaluated in terms of its RMSE and computation time) are illustrated with three DCS (PM1/ EM1, PM2/EM2, and PM5/EM5) models in Table II.

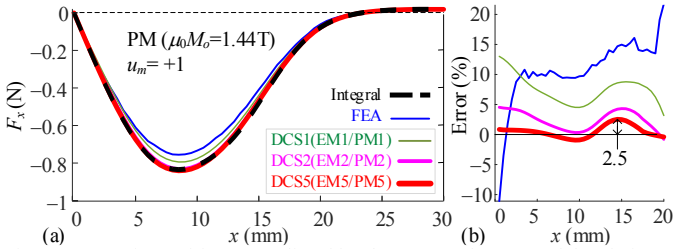

Fig. 4. Comparison of forces predicted by the DCS and FEA models relative to integral solutions. (a) Computed forces. (b) Numerical errors.

TABLE II. PARAMETERS USED IN NUMERICAL VERIFICATION

EM: J_o= 4 A/mm^2 (d_w=0.5 mm), a_o=10, a_i=4, l_e=5 mm.
PM and its DCS models are given in Table I

DCS	VCD, N_k = $n_{Axi} \times n_{Rad} \times n_{Circ}$	Volume v_k (mm^3)	RMSE (mN)	Comp. Time (s)
EM1	1×1×10	131.9	31.3	0.065
EM2	2×2×20	16.49	10.7	0.29
EM5	5×5×50	1.056	4.82	7.1
Numerical Integral (AbsTol=RelTol=10^{-3})			Exact	2,133.6
FEA (Tetrahedron 239,246 elements)			51.6	427

Solution Domain	PM-pair	EM-pair	Air
	51,848 (21.7%)	42,754 (17.9%)	144,644 (60.4%)

A.3 Discussion of results

Some observations can be revealed from the findings presented in *Sections A.1* and *A.2*:

– With as small as N_K=N_k=10 elements, the DCS models predict relatively accurate the PM MFD and forces between the EM-pair and PM-pair; both the (RMSE, Max) errors are smaller than FEA [Tables (I, II); Figs. (2, 4)]. The DCS model accuracy can be improved by refining the discretization which increases the time from 39ms to 86ms (250 SCDs) for computing the MFD, and from 65ms to 7.1s (1250 VCDs) for calculating the force. The DCS5 models and the exact solutions yield nearly an identical prediction of the MFD (Fig. 2) and force (Fig. 4). Based on this study, the (PM, EM) are modeled with N_K=5×50 SCDs and N_k=5×5×50 VCDs in *Section B*.

– The DCS model is time-efficient (a 3-order improvement over FEA) and potentially can be further optimized for real-time computation. The exact solutions take nearly 6

hours to calculate the Lorentz force from the volume integral (18a). Although COMSOL can automatically mesh an FEA model, a large percentage (80%, 60%) of its free meshed tetrahedrons (151,835, 239,246) for the (MFD, force) computation is used in the air domain. The need to include the air domain not only is time-demanding (7.9s for MFD and 427s for force) but also results in noisy solutions as revealed in the error plots in Figs. 2 and 4(b).

B. Design of a Three-DOF Planar Motor

The geometrical constraints and parametric effects on the force/torque of a prototype 3-DOF planar motor (Figs. 1a, 5) are analyzed in *Sections B.1* and *B.2*, respectively.

For specified d_c, r_l and r_u,

C1: $r_l + (r_p + d_c) \le r_s \le r_u - r_p$

C2: $r_l + a_o \le r_r \le r_u - (a_o + d_c)$

C3: $r_p \le r_s \sin\pi/(2N_p)$

C4: $a_i < a_o \le r_r \sin(\pi/N_e)$

For specified h_u and g_h,

C5: $l_p + l_e + g_z \le (h_u - g_h)/2$

Ensure some PM-EM overlap,

C6: $|r_s - r_r| \le r_p + a_o$

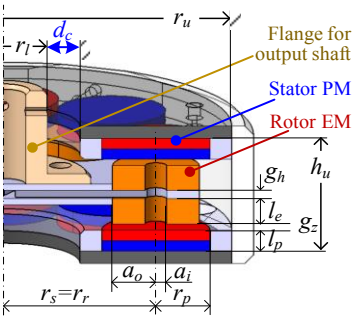

Fig. 5. CAD model of a prototype planar motor illustrating its geometrical constraints and design parameters.

B.1 Geometrical Constraints on the PMEM Layouts

The geometrical constraints imposed on the PM/EM layout are described by the inequalities (C1) to (C5) in Fig. 5 where $\pm d_c$ is the specified (X_c, Y_c) range bounded by the flange (radius r_l) and enclosure (r_u, h_u). The criterion (C6) limits $|r_s - r_r|$ to maintain some overlaps between the PMs and EMs preventing trivial motion singularities. In practice, (r_p; a_o, a_i) depend on the forces/torque specified for an application, which may result in an increase in (r_s, r_r) accordingly at the expense of a larger overall enclosure (r_u and/or h_u). To help visualize, Fig. 6 numerically illustrates the constraints imposed on the stator-PMs (r_p, l_p, r_s, $2N_p$) and rotor-EMs (a_o, l_e, r_r, N_e) for the bounds (r_l=10, r_u=52.5) mm and motion range ($\pm d_c$=7.5mm).

The bounding curves (Fig. 6) are derived by substituting the upper limits of the outer radii (C3, C4) of the (PM, EM) into (C1, C2). The regions satisfying the two resulting constraints [(C3) in (C1), (C4) in (C2)] are denoted by the (red, blue)-colored pairs of arrows ($\Rightarrow$,$\Leftarrow$) in Fig. 6. The lower/upper curves intercept at (27.5, 35)mm constraining the (PM, EM) layouts. The ($r_s \approx r_r$=30mm) configuration indicated as ① (r_s=28.3, $2N_p$=8) and ❷ (r_r=30mm, N_e=6) in Fig. 6 is used to calculate the largest (r_p, a_o) from (C3, C4).

B.2 Parametric Effects on Force/Torque Performance

For a given [**A**], the inverse model (7a~e) computes the current inputs (N_e>3) for a specified set of forces/torque. The parametric effects on ($\mathbf{AA}^T$) and hence the forces/torque are illustrated with N_e (6, 9); both with $2N_p$=8 and r_s=r_r=30mm (black dashed line in Fig. 6). The eigenvalue decomposition results are summarized in Figs. 7(a, b) and 8 and in Table III.

The 3D heat maps (Fig. 7a) graphically compare the effects of N_e(6, 9) on E_F and E_V indicators (14a, b) in 1st and 2nd rows for N_e=6 (left) and N_e=9 (right), where the vertical layers correspond to four θ values (0°: 15°: 45°) for N_e=6 and eight θ values (0°: 5°: 35°) for N_e=9. Because the EMs are equally spaced at 360°/N_e and move as a rigid body relative to the stator-PMs spaced at 360°/($2N_p$), the forces and torque on the rotor are periodic and symmetric about a radial axis through the EM center. To avoid repetition, the E_F and E_V data (Fig. 7a) are organized and plotted along r_c for four α values (0°, 45°, 90°, 135°) in Fig. 7(b) where

$$r_c = \sqrt{X_c^2 + Y_c^2} \text{ and } \alpha = \tan^{-1} Y_c / X_c$$

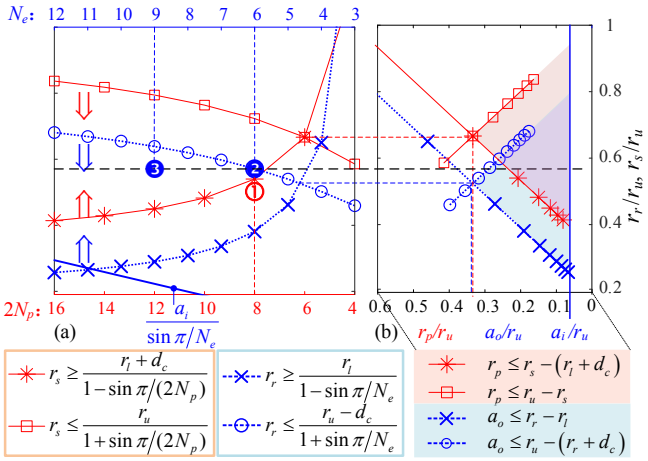

Fig. 6. Effects of geometrical constraints on the layout configurations and design parameters of the stator-PMs and rotor-EMs.

TABLE III. NUMERICAL RESULTS

Common parameters:
Geometry (mm): r_l=r_s=30, l_e=l_p=5, g_z=1.5, g_h=2.
N_p=8, **PM** (r_p=11.5 mm, B_o=1.44 T), **EM** (a_i=4 mm, J_o=4 A/mm²).

EM	N_e: a_o (mm²), V_e (mm³), f_o (N)=$B_o J_o V_e$, τ_o (Nm)=$r_p f_o$	
	6: 15.0, 3283, 18.9, 0.22	**9:** 10.3, 1402, 8.07, 0.09

Fig. 9	E_F	E_V	E_F	E_V
Max	❶ 0.8251	③ 0.0683	❶ 0.9714	③ 0.1904
Min	❷ 0.7231	④ 0.0318	❷ 0.7796	④ 0.0016

Inverse Model Eq. (12) with $\mathbf{F} = [\bar{f}_X \ \bar{f}_Y \ \bar{\tau}_Z]^T = [1\ 1\ 1]^T$

	N_e=6		N_e=9	
	(r_c, α, θ)	$\|\mathbf{u}\|_2^2$	(r_c, α, θ)	$\|\mathbf{u}\|_2^2$
Best	(6, 0, 30)	28.43	(6.5, 0, 0)	19.15
	u: (–0.49, –2.00, –1.66, 1.38, –3.10, **3.16**)		**u:** (–0.49, –0.66, 0.85, 1.09, –1.83, 1.11, 0.94, **–2.82**, 1.79)	
Worst	(7.5, 0, 0)	80.37	(5.5, 0, 20)	954.3
	u: (–1.10, 5.89, 2.26, –1.20, 1.79, **–5.89**)		**u:** (4.98, 14.7, 10.5, 11.0, –4.50, –3.71, –11.1, **–17.5**, –3.99)	

For ease of comparison, both color bars (Fig. 7a) are presented in $\log_{10}$ scale from blue to yellow, designating the best to worst measures. The (r_c, α, θ) locations at which the worst and best (E_F, E_V) measures of the two designs (N_e =6, 9) are identified in Figs. 7(a, b): ❶ for worst (or max E_F), ❷ for best (or min E_F), ③ for best (or max E_V), and ④ for worst (or min E_V). As shown in Figs. 7(a, b), $E_{F(\max)}$ and $E_{V(\min)}$ occur at the same r_c while the locations of $E_{F(\min)}$ and $E_{V(\max)}$ differ but close. To help visualize, these "best" and "worst" $\mathbf{AA}^T$ ellipsoid indicators are displayed in Fig. 8:

N_e =6: Worst $\mathbf{AA}^T$ at r_c=±7.5mm. Best $\mathbf{AA}^T$ at r_c=±6 mm (average of $E_{F(\min)}$ at ±7 and $E_{V(\max)}$ at ±5).

N_e =9: Worst $\mathbf{AA}^T$ at r_c=±5.5mm. Best $\mathbf{AA}^T$ at r_c=±6.5mm (average of $E_{F(\min)}$ at ±7.5 and $E_{V(\max)}$ at ±5.5).

As shown in Fig. 8(a, b), the loci connecting the best (or worst) ellipsoids can be described by a helix. The effects of the best and worst $\mathbf{AA}^T$ on the optimal **u** (12) are analyzed in Table III where the inverse solution solves for **u** at the locations (denoted by the boxes in Fig. 8) to meet the specified force

vector $\left[\bar{f}_X = 1 \;\; \bar{f}_Y = 1 \;\; \bar{\tau}_Z = 1\right]^{\mathrm{T}}$. As shown in Fig. 8 comparing the manipulability ellipsoid two N_e (6, 9), the largest radii of both layouts incline to π. The manipulability ellipsoid of the 8PM/6EM layout are uniform over the entire operating range except at its boundary. However, the 8PM/9EM layout exhibits a wide range of ellipsoid volume/flattening ($E_{V(max)}/E_{V(min)}$=119, $E_{F(max)}/E_{F(min)}$=1.25), as a result, demanding a significantly lager currents at the "worst" locations (Table III).

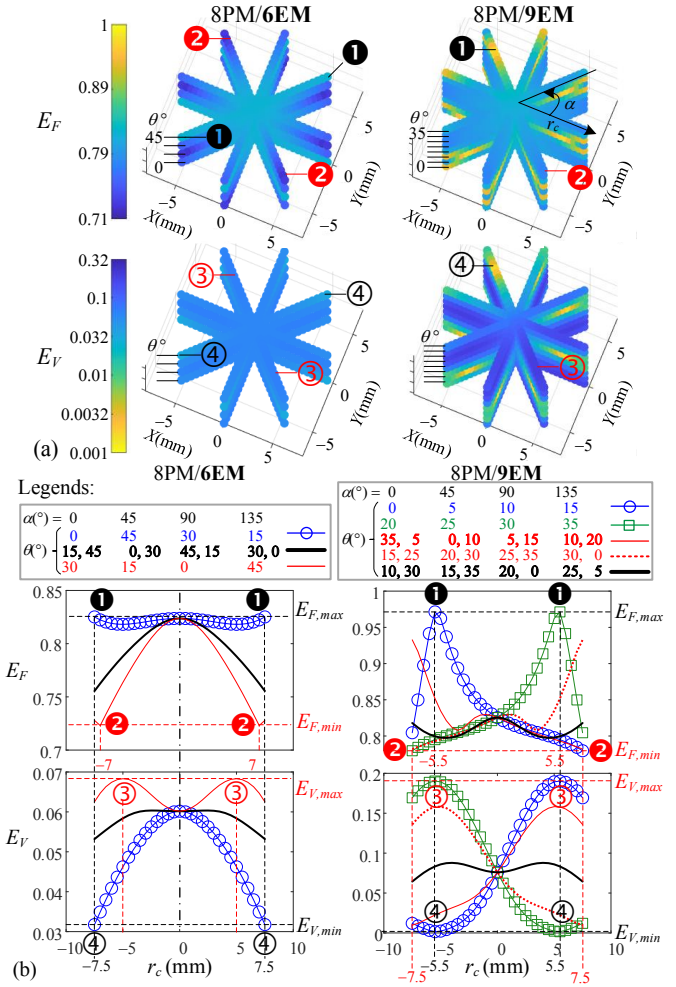

Fig. 7. Ellipsoid indicators: E_F (1st row) and E_V (2nd row) for N_e=6 (left) and N_e=9 (right). (a) 3D heat maps. (b) (E_F, E_V) along radial paths.

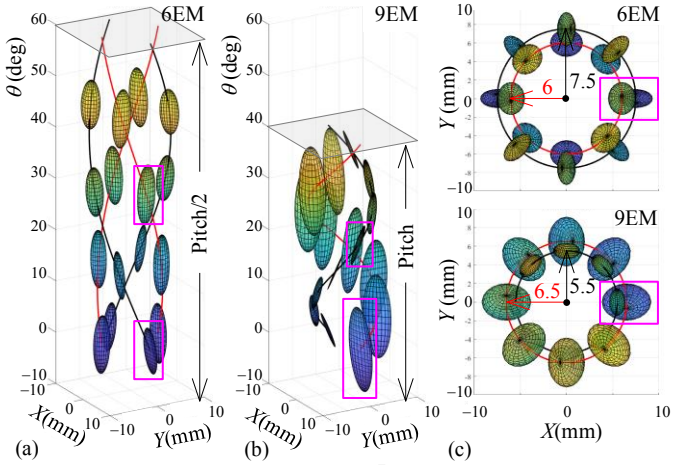

Fig. 8. Loci of the best/worst (E_F, E_V) of $\mathbf{AA}^{\mathrm{T}}$ ellipsoids. (a) N_e=6. (b) N_e=9. (c) Plan views: N_e=6 (top) and N_e=9 (bottom).

IV. Conclusion

A field-based method employing the DCS models as a design tool for analyzing the parametric effects on the forces/torque of the 3D planar motor has been presented. The findings, which have been verified by comparing the (MFD, force) results with exact solutions and with the commercial FEA, demonstrate that the DCS models are computationally accurate (RMSE: 0.093mT, 4.82mN) and time-efficient (0.086s, 7.1s) representing significant improvements over FEA of (RMSE: 7.9mT, 51.6mN) and (23s, 423s). With the magnetic forces/torque derived in closed form, different design configurations can be analyzed using singular value decomposition where their parametric effects can be graphically visualized using manipulability ellipsoids to identify the "best" and "worst" forces/torque performance. While illustrated with two different N_e(6, 9) EMs of a motor design, other parametric effects on motor performance can be analyzed similarly.

References

[1] K.-M. Lee, J. Guo, "Kinematic and dynamic analysis of an anatomically based knee joint," *J. Biomech.*, vol. 43, no. 7, pp. 1231-1236, 2010.

[2] D. Wang, K.-M. Lee, J. Guo, C.-J. Yang, "Adaptive knee joint exoskeleton based on biological geometries," *IEEE/ASME Trans. Mechatronics (T MECH).*, vol. 19, no. 4, pp. 1268-1278, 2014.

[3] Y. Ren, Y.-N. Wu, C.-Y. Yang, T. Xu, R. L. Harvey, L.-Q. Zhang, "Developing a wearable ankle rehabilitation robotic device for in-bed acute stroke rehabilitation," *IEEE Trans. Neural Syst. Rehabil. Eng.*, vol. 25, no. 6, pp. 589–596, 2017.

[4] J. Jiang, W. Li, K.-M. Lee, "A novel pantographic exoskeleton based collocated joint design with applications for early stroke rehabilitation," *IEEE/ASME T MECH*, v. 25, n. 4, pp. 1922-1932, 2020.

[5] H.-S. Cho, C.-H. Im, H.-K. Jung, "Magnetic field analysis of 2-D permanent magnet array for planar motor," *IEEE Trans. Magnetics (T MAG)*, vol. 37, no. 5, pp. 3762-3766, 2001.

[6] H.-S. Cho, H.-K. Jung, "Analysis and design of synchronous permanent-magnet planar motors," *IEEE Trans. Energy Convers.*, vol. 17, no. 4, pp. 492-499, 2002.

[7] S. Zhang, X. Dang, K. Wang, J. Huang, J. Yang, G. Zhang, "An analytical approach to determine coil thickness for magnetically levitated planar motors," *IEEE/ASME T MECH*, vol. 22, no. 1, pp. 572-580, 2017.

[8] W. Min, M. Zhang, Yu. Zhu, B. Chen, G. Duan, J. H, W. Y, "Analysis and optimization of a new 2-D magnet array for planar motor," *IEEE T MAG*, vol. 46, no. 5, pp. 1167-1171, 2010.

[9] J. Lee, S.-W. Lee, K. Kim, J. Lee, "Multi-material topology optimization of magnetic actuator with segmented permanent magnets," *IEEE T MAG*, vol. 54, no. 7, pp. 1-6, 2018.

[10] J. Lim and K.-M. Lee, "Distributed multilevel current models for design analysis of electromagnetic actuators," *IEEE/ASME T MECH*, vol. 20, no. 5, pp. 2413-2424, 2015.

[11] C.-Y. Lin, K.-M. Lee, B. Hao, "Distributed current source method for modeling magnetic and eddy-current fields induced in nonferrous metallic objects," *IEEE/ASME T MECH*, vol. 23, no.3, pp. 1038-1049, 2018.

[12] J. Lim, C.-Y. Lee, S. Choi, J.-H. Lee, K.-S. Lee, "Design optimization of a 2G HTS magnet for subsonic transportation," *IEEE Trans. Appl. Supercond.*, vol. 30, no. 4, pp. 1-5, 2020.

[13] V.Puumala, J.Tampio, S. Suuriniemi, L. Kettunen, "Force decomposition for magnetic actuators," *IEEE T MAG*, vol. 53, no. 3, pp. 1-7, 2017.

[14] S. Lee, H. Kim, H. Son, "Moment method based distributed multipoles for modeling magnetic materials in 2D and 3D magnetostatics," *Comput. Meth. Appl. Mech. Eng.*, vol. 393, 2022.

[15] T. Yoshikawa, "Manipulability of Robotic Mechanisms," *Int. J. of Robotics Research.* vol. 4, no. 2, pp. 3-9, 1985.

[16] K.-M. Lee, H. Son, "Distributed multipole model for design of permanent-magnet-based actuators," *IEEE T MAG*, vol. 43, no. 10, pp. 3904-3913, 2007.